JACS
JOURNAL OF THE AMERICAN CHEMICAL SOCIETY
pubs.acs.org/JACS
Article

# Spatiochemical Segregation in Porous Lithium–Metal Interphases

Weilai Yu, Hao Lyu, Donglin Li, Kuan-Yu Lin, Jacob Florian, Yukio Cho, Xin Xu, Yuelang Chen, Hongchang Hao, Chengyi Xu, Dennis Nordlund, Jagjit Nanda, Jian Qin, Yi Cui,* and Zhenan Bao*

Cite This: J. Am. Chem. Soc. 2026, 148, 24084–24095
Read Online
ACCESS | Metrics & More | Article Recommendations | Supporting Information

**ABSTRACT:** The solid–electrolyte interphase (SEI) on lithium metal forms through electrolyte reduction at a dynamically evolving metal surface, yet how its chemistry and spatial organization develop during lithium plating and stripping remains poorly understood. Here, using a 1,2-dimethoxyethane (DME)/1 M lithium bis(fluorosulfonyl)imide (LiFSI) electrolyte system, we show that three-dimensional lithium growth drives spatiochemical segregation of interphase products into chemically heterogeneous domains that are mechanically reorganized during stripping into a porous electrolyte-retaining framework. Correlative X-ray photoelectron spectroscopy, scanning electron microscopy, nanoscale secondary ion mass spectrometry (NanoSIMS), and synchrotron X-ray absorption spectroscopy reveal that $FSI^-$-derived inorganic species, dominated by LiF, become enriched in regions spatially decoupled from oxygen-containing phases near the lithium surface. Stripping-induced contraction compacts these chemically distinct domains into confined intergranular volumes, where supersaturation promotes precipitation and consolidation, yielding a porous SEI that retains electrolyte-derived species within a buried pore network beyond the reach of surface-sensitive probes. Spatiochemical segregation thus couples interfacial reaction pathways to lithium chemo-mechanics, dictating interphase composition, architecture, and permeability. These findings establish a chemo-mechanical framework for SEI evolution and suggest strategies to mitigate electrolyte retention and interphase instability in lithium–metal batteries.

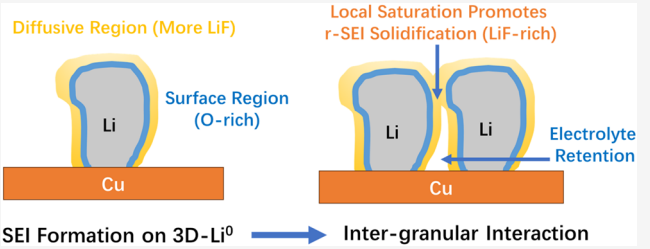


## 1. INTRODUCTION

Lithium–metal batteries (LMBs) are widely regarded as a cornerstone of next-generation energy storage, offering theoretical energy densities approaching 500 Wh $kg^{-1}$.[1] Unlike lithium-ion batteries that rely on intercalation hosts such as graphite, LMBs operate through direct lithium plating and stripping, leading to large volume changes and dynamic surface restructuring at the anode.[2] Combined with the extremely low electrochemical potential of lithium (−3.04 V vs NHE), this highly reactive and morphologically unstable interface continuously drives electrolyte decomposition and the formation of a solid–electrolyte interphase (SEI).[3,4]

In conventional lithium-ion batteries, the SEI forms as a nanometer-scale passivation layer that electrically isolates the electrode while permitting ion transport.[5] On lithium metal, however, SEI formation is intrinsically dynamic. A native SEI forms spontaneously on Li foil, while our previous work showed that even a bare copper current collector develops a passivating Cu-SEI when polarized to lithium metal potential.[6] Subsequent lithium deposition creates a distinct Li-SEI on the growing metal surface, and lithium stripping leaves behind a residual SEI (r-SEI) that remains attached to the current collector.[7,8] These sequential interfacial states evolve continuously during cycling, producing chemically and structurally distinct interphases whose transformation is inseparable from lithium–metal growth and removal.[9]

Despite major advances in electrolyte design that have enabled Coulombic efficiencies exceeding 99%,[10−13] a mechanistic understanding of how SEI chemistry, nanoscale structure, and lithium morphology coevolve during cycling remains incomplete. In particular, how electrolyte-derived species partition among Cu-SEI, Li-SEI, and r-SEI, and how this partitioning couples to lithium plating and stripping, is still poorly understood.[14] The spatial redistribution of SEI components can strongly influence ionic transport, porosity, and mechanical integrity, which in turn govern parasitic reactions, dead-lithium formation, and long-term reversibility.[15,16] Elucidating the spatiochemical and morphological dynamics of SEI evolution is therefore essential for establishing rational principles to control electrolyte stability, suppress interfacial degradation, and unlock the full potential of lithium–metal batteries.

To address this knowledge gap, we integrate complementary surface-, lateral-, and depth-resolved measurements to track how lithium–metal interphases reorganize during cycling.

Received: February 28, 2026
Revised: April 21, 2026
Accepted: May 4, 2026
Published: June 1, 2026

**Scheme 1. (a) Charging−Discharging Protocol Used to Probe the Temporal Evolution of the SEI in Li-Metal Batteries. Cu-SEI is first formed by holding a Cu electrode at 0 V versus $Li^0$ (0 $V_{Li}$) for 3 h in a Li|Cu half-cell. Lithium metal is then electroplated at −0.5 mA for 2 *h* to generate Li-SEI-1. This is followed by five galvanostatic stripping/plating cycles at ±0.5 mA with *a* capacity cutoff of 1.0 mAh, producing residual SEI (r-SEI) of varying cycle numbers. A final plating step yields Li-SEI-6. All experiments were performed using a DME/1 M LiFSI electrolyte. (b) Schematic comparison of Cu-SEI, Li-SEI, and r-SEI, highlighting their distinct structural and compositional characteristics.**

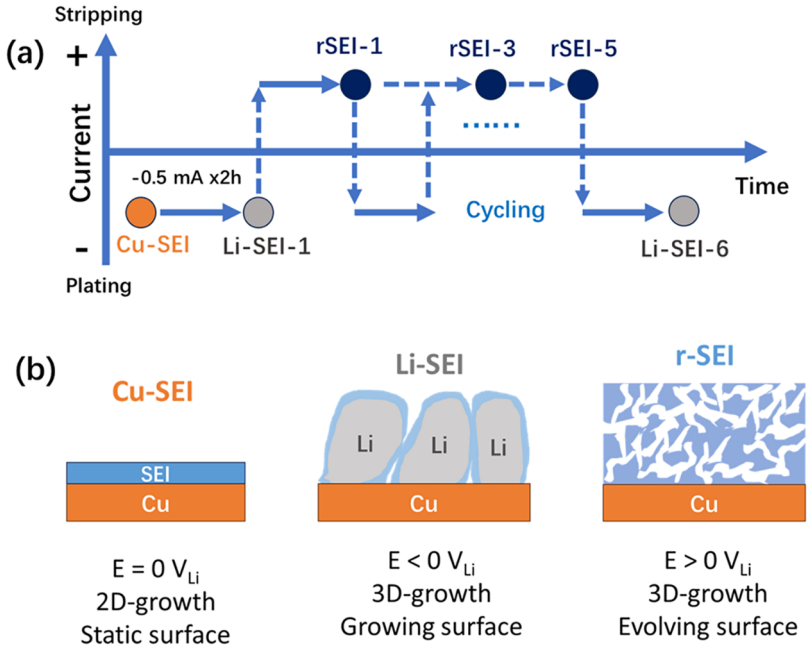


Quantitative X-ray photoelectron spectroscopy (XPS) on rigorously salt-free surfaces resolves distinct compositional signatures for Cu-SEI, Li-SEI, and the residual SEI (r-SEI) across repeated plating and stripping. Nanoscale secondary ion mass spectrometry (NanoSIMS) maps the lateral chemical landscape and reveals spatiochemical segregation of anion-derived products on freshly plated lithium, while soft- and tender-energy synchrotron X-ray absorption spectroscopy (XAS) probes buried interphase chemistry and detects electrolyte species retained within the evolving interphase. Integrating these correlative data sets with morphological analysis by scanning electron microscopy (SEM), we establish a chemo-mechanical framework in which interphase architecture is governed by phase segregation under moving lithium boundaries. Three-dimensional lithium growth partitions reaction products into laterally heterogeneous domains, and stripping-induced intergranular contraction compacts and consolidates these domains into a porous, electrolyte-retaining r-SEI. This segregation−confinement mechanism links interfacial reactions to lithium morphology and cycling dynamics and provides design principles to mitigate electrolyte retention and interphase instability.

## 2. RESULTS AND DISCUSSION

### 2.1. Cycling Produces Distinct Chemical Fingerprints of Cu-SEI, Li-SEI, and r-SEI

To compare the compositional characteristics of different SEI types, we categorize them into three groups: Cu-SEI, Li-SEI, and r-SEI (Scheme 1a). A baseline electrolyte composed of 1 M lithium bis(fluorosulfonyl)imide (LiFSI) salt dissolved in 1,2-dimethoxyethane (DME) solvent (DME/1 M LiFSI) was used throughout this study, reaching an expected CE of ∼98% upon cycling of Li|Cu half-cells (Figure S1). In a Li|Cu half-cell, *a* thin Cu-SEI forms initially to passivate the copper current collector when its potential ($E_{Cu}$) matches that of lithium metal (0 $V_{Li}$).[17] As $E_{Cu}$ becomes more negative than 0 $V_{Li}$, lithium metal deposits on the copper surface, disrupting the Cu-SEI and forming a new Li-SEI on the freshly plated lithium. Although both Cu-SEI and Li-SEI arise from electrolyte decomposition driven by the highly reducing potential of lithium metal, they differ fundamentally in the nature of their formation interfaces: Cu-SEI forms on a static, two-dimensional (2D) copper surface, whereas Li-SEI develops on a dynamic, three-dimensional (3D) lithium metal surface (Scheme 1b). Upon lithium stripping during discharge, a r-SEI remains on the copper substrate. With continued cycling and complete lithium removal, this r-SEI transforms into a continuously evolving, 3D-porous structure capable of interacting with subsequently redeposited lithium.[7] The SEI formed at a specific cycle number ($x$) is denoted as "SEI-$x$". To clarify the key trends, we discuss the XPS results along three compositional axes: (i) oxygen-containing species, (ii) anion-derived LiF, and (iii) sulfur-containing species associated with progressive FSI decomposition.

After SEI formation, systematic XPS analysis was performed to investigate the compositional characteristics of each SEI type. Following cell disassembly, all samples on the copper substrate were carefully washed with pure DME solvent. As shown in Figure S2, the F 1s XPS spectra of all SEI samples revealed a single peak corresponding to LiF at a binding energy (BE) of 684.8 eV, confirming the effectiveness of the washing protocol in producing clean sample surfaces free of electrolyte salts. This step ensured reliable XPS analysis by preventing artificial LiF formation from LiFSI salt due to X-ray irradiation or $Ar^+$ sputtering.[18,19]





https://doi.org/10.1021/jacs.6c04430
J. Am. Chem. Soc. 2026, 148, 24084−24095

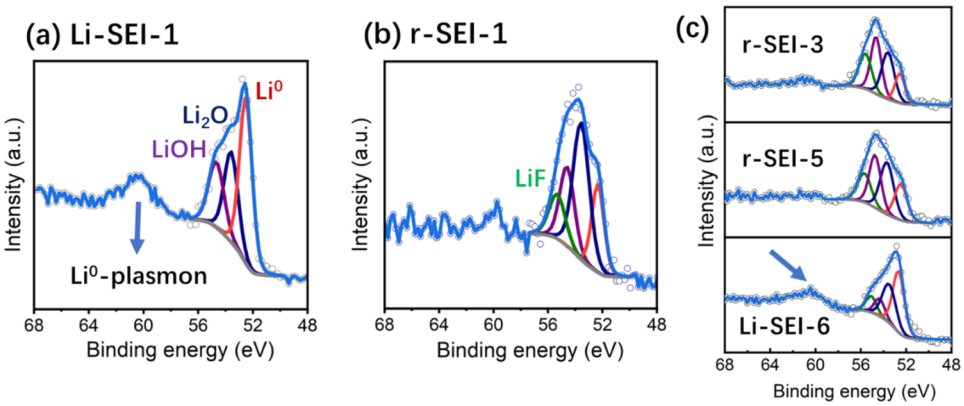


**Figure 1.** Comparison of high-resolution Li 1s XPS surface spectra for (a) Li-SEI-1, (b) r-SEI-1, and (c) r-SEI-3, r-SEI-5, and Li-SEI-6 (from top to bottom). The Li 1s peaks are deconvoluted into components corresponding to metallic $Li^0$ or LiH (red), $Li_2O$ (blue), LiOH (purple), and LiF (green).

We first performed a side-by-side comparison of the Li 1s spectra for Li-SEI and r-SEI formed at different cycles. As shown in Figure 1a, a broad $Li^0$ plasmon peak near ∼ 60 eV was observed exclusively in Li-SEI-1, but not in r-SEI-1, corresponding to a sharp $Li^0$ peak at ∼52.5 eV attributed to metallic lithium.[20] These Li-metal features persisted even after extended $Ar^+$ sputtering and were further confirmed by XPS analysis of a Li-metal foil reference (Figures S3 and S4). Constraining the full width at half-maximum (fwhm) to 1.1−1.4 eV, the Li 1s spectrum of Li-SEI-1 was deconvoluted into two distinct peaks at ∼53.6 and 54.7 eV, assigned to $Li_2O$ and LiOH, respectively.[20] We note that LiF may not be distinctly resolved in the Li 1s spectra due to overlap with other Li-containing species (e.g., LiOH), and is therefore more reliably identified via the F 1s spectrum. Due to the surface sensitivity of XPS, these results indicate that photoelectrons originating from the underlying $Li^0$ metal can still be detected through the overlying parasitic SEI species, such as oxides and hydroxides. Notably, the relative intensity of the LiOH peak decreased progressively with sputtering, suggesting a higher concentration of $Li_2O$ in the inner regions of Li-SEI-1 (Figure S3). A similar depth-dependent increase in $Li_2O$ signal was observed in the sputtering profile of a Li-metal foil covered with its native SEI (Figure S4).

In contrast, the absence of the $Li^0$ plasmon peak in r-SEI-1 confirms the effective removal of metallic $Li^0$ from the surface, although inactive $Li^0$ may still reside within the bulk of the sample (Figure 1b).[21] The shoulder at ∼52.5 eV is likely attributed to LiH, consistent with the low electronegativity of hydrogen.[22] Similar to Cu-SEI, a pronounced peak at ∼55.5 eV, assigned to LiF, is also observed in r-SEI-1 (Figure S3). Notably, the $Li_2O$ peak shows the highest intensity at the surface but gradually approaches the intensity of LiOH with increasing sputtering depth, suggesting a more even distribution of these species in the inner regions of r-SEI-1.

During subsequent cycles, $Li^0$ plasmon peaks remained absent in all r-SEI samples but reappeared in Li-SEI-6 (Figure 1c). This observation is consistent with previous reports suggesting that electroplated Li metal can eventually grow through the accumulated r-SEI layer.[7,8] The r-SEI formed after the third and fifth cycles exhibited similar deconvoluted peak distributions for LiF, LiOH, $Li_2O$, and LiH, which remained largely unchanged upon sputtering—indicating a compositionally homogeneous r-SEI throughout its depth (Figure S3). In contrast, while LiF was still detected in Li-SEI-6, its relative intensity was lower compared to r-SEI samples, accompanied by a notable increase in $Li_2O$ content. These findings highlight that careful deconvolution of high-resolution Li 1s XPS spectra can reveal distinct compositional signatures that differentiate various SEI types.

We next systematically evaluated the XPS sputtering profiles of nonlithium elements. The etching depth achieved by a 3 min $Ar^+$ sputtering process was ∼10 nm. In the O 1s spectra, Cu-SEI showed comparable peak intensities for $Li_2O$ (528.2 eV) and LiOH (∼531 eV) throughout the sputtering duration. In contrast, Li-SEI exhibited a gradual increase in the relative intensity of the $Li_2O$ peak, suggesting a higher concentration of $Li_2O$ closer to the underlying $Li^0$ surface—consistent with the Li 1s data (Figure S5).[10,23] For all r-SEI samples, however, LiOH remained more prominent even after the sputtering, again indicating a different oxygen species distribution in the residual SEI.

Because the surface C 1s spectra were dominated by adventitious carbon peaks, we instead analyzed the post-sputtering C 1s profiles to gain insight into the organic (carbon-containing) species present in the various SEIs (Figure S6). The Cu-SEI showed an enrichment of diverse organic functional groups, including $Li^+$-$C^-$, C−C/H, C−O, C═O, and $-CO_3$ (Figure S6a). In contrast, the organic components of both Li-SEI and r-SEI were primarily composed of $Li^+-C^-$ and C−C bonds, with comparable peak intensities. This suggests the formation of alkyl lithium (LiR, R = $C_xH_y$) or polyolefin ($C_xH_y$) species resulting from DME decomposition. Minor C−O bonds were consistently detected in all r-SEI samples, becoming more prominent with increased cycle number—possibly indicating the formation of alkoxy lithium (LiOR) or poly(ethylene oxide) (PEO) species.[24] Notably, carbonate ($-CO_3$) signals (∼290 eV) were absent in both Li-SEI and r-SEI.

Comparison of the S 2p sputtering profiles revealed major and minor doublet peaks corresponding to $Li_2S$ (∼160 eV) and $-SO_x$ species (∼167 eV), respectively—representing fully and partially reduced sulfur species derived from the $FSI^-$ anion (Figure S7). The $-SO_x$ species were more abundant at the surface of all SEI samples, whereas only Li-SEI-1 exhibited a dominant $Li_2S$ signal after sputtering. The N 1s sputtering profiles showed relatively noisy signals, reflecting the low abundance of nitrogen-containing species across all SEI types




https://doi.org/10.1021/jacs.6c04430
J. Am. Chem. Soc. 2026, 148, 24084−24095

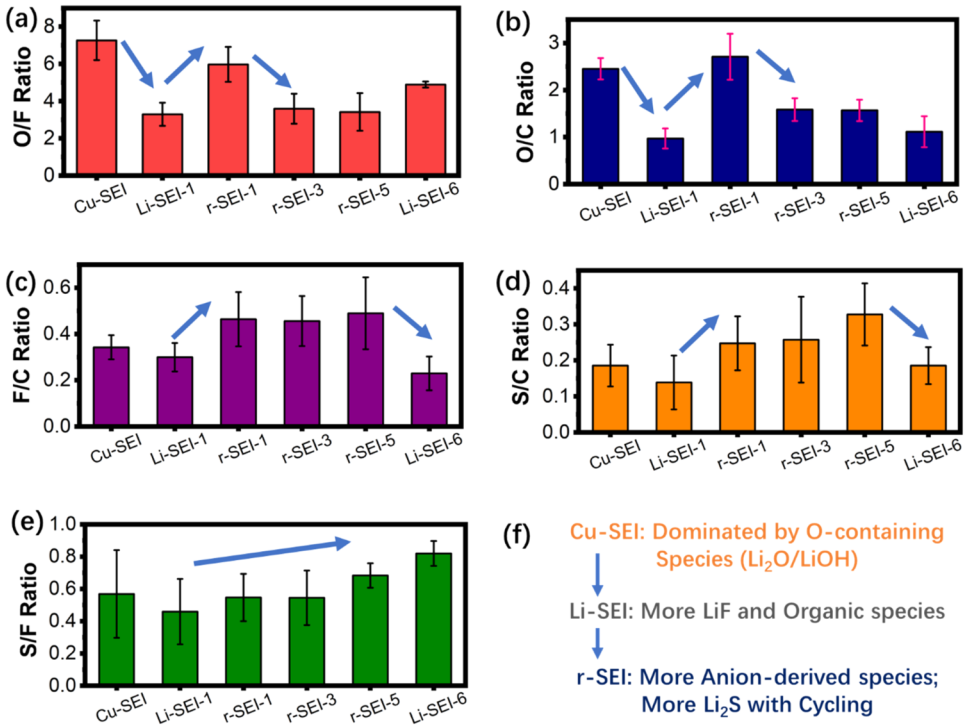


**Figure 2.** (a) Comparison of atomic ratios for (a) O/F, (b) O/C, (c) F/C, (d) S/C, and (e) S/F across different SEI types (Cu-SEI, Li-SEI, and r-SEI) at various cycle numbers. XPS data were collected after 1 min of $Ar^+$ sputtering at 1 kV to enable reliable atomic quantification. Statistical analysis was based on measurements taken from five distinct regions per sample. Arrows indicate notable changes in atomic ratios at different plating−stripping stages of the LMBs. (f) Summary of key compositional distinctions between different types of SEI.

(Figure S8). Nonetheless, two peaks of comparable intensity were observed at ∼398 and ∼396 eV, assigned to N−$SO_x$ and $Li_3N$, respectively. Together, the S 2p and N 1s spectra indicate that even partially decomposed $FSI^-$ fragments contribute to SEI formation throughout both surface and bulk regions.

### 2.2. Anion-Derived Species Progressively Enrich during Cycling

Since all SEI samples exhibited similar spectroscopic features across various elements, we next compared their atomic ratios. To minimize the influence of surface adventitious carbon, XPS data collected after 1 min of sputtering were used as a consistent reference depth across samples, balancing removal of surface contamination with avoidance of excessive beam-induced modification and enabling more representative analysis of both organic and inorganic species. To reduce measurement variability, atomic ratios were averaged across five different locations per sample, as summarized in Figure 2.[25]

Overall, the XPS data highlight distinct distributions of three primary components across different SEI types: oxide/hydroxide (O), organic species (C), and anion-derived species (S/F). Four key comparisons can be made to reveal how SEI composition evolves during Li-metal cycling, providing a simplified framework to interpret the compositional evolution of Cu-SEI, Li-SEI, and r-SEI:

1. **Cu-SEI vs Li-SEI-1**: Cu-SEI, formed on a static Cu surface, is dominated by oxide/hydroxide (O-containing) species, with fewer organic and anion-derived species. In contrast, Li-SEI-1, formed on actively plating Li metal, exhibits a higher concentration of organic species and LiF (Figure 2a,2c), indicating compositional shifts due to the dynamic SEI growth.
2. **Li-SEI-1 vs r-SEI-1**: Comparing SEI formed during initial plating (Li-SEI-1) to that after stripping (r-SEI-1) reveals stripping's impact on SEI composition. Post-stripping, r-SEI-1 shows an increase in oxygen content, aligning with Cu-SEI, likely due to partial exposure of the underlying Cu. Additionally, r-SEI-1 displays higher F/C and S/C ratios, indicating enhanced incorporation of FSI-derived fluorine- and sulfur-containing species (Figure 2c,d). This increase reflects relative enrichment arising from preferential removal of more soluble organic (C-containing) species and retention of less mobile inorganic components.
3. **Evolution of r-SEI with Cycling**: With ongoing cycling, r-SEI shows decrease in O/F and O/C ratios with no substantial change from r-SEI-3 to r-SEI-5, suggesting a more uniform SEI structure, with anion-derived species increasingly dominant over oxygen species. There is also a gradual increase in sulfur-containing species, indicating a continuous incorporation of sulfur species (−$SO_x$/$Li_2S$) within r-SEI across cycles (Figure 2e).
4. **Li-SEI-6 vs r-SEI-5**: In later cycles, Li-SEI-6 shows a marked increase in O/F and reductions in O/C, F/C, and S/C ratios compared to r-SEI-5. This shift, consistent with Li 1s data, suggests that additional Li plating exposes fresh Li surface, leading to higher contents of oxide, hydroxide, and organic species in the Li-SEI.

Notably, the S/F ratio in Li-SEI-1 rises progressively from <0.5 to ∼0.8 by Li-SEI-6, approaching the stoichiometry of LiFSI salt. The increase in S/F ratio reflects progressive sulfur




https://doi.org/10.1021/jacs.6c04430
J. Am. Chem. Soc. 2026, 148, 24084−24095

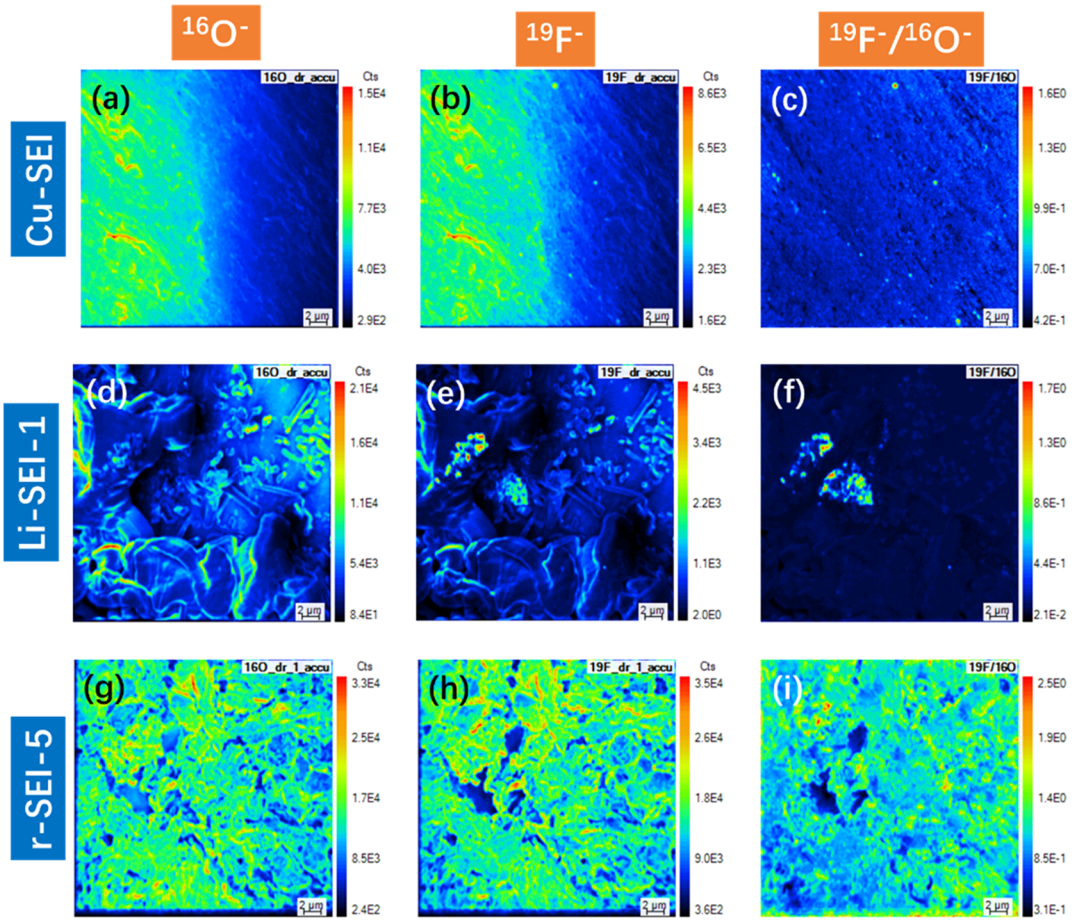


**Figure 3.** Comparison of nanoscale secondary ion mass spectrometry (NanoSIMS) 2D imaging for (a–c) Cu-SEI, (d-f) Li-SEI-1, and (g–i) r-SEI-5 samples, mapping the spatial distributions of (a, d, g) $^{16}O^-$, (b, e, h) $^{19}F^-$ ions, as well as the normalized (c, f, i) $^{19}F^-/^{16}O^-$ ratio.

enrichment, with LiF forming preferentially at early stages, and is consistent with a mixture of FSI-derived sulfur-containing species ($-SO_x/Li_2S$) retained within the SEI matrix during prolonged cycling. Thus, the SEI composition transitions from an oxide-rich Cu-SEI to an organic- and LiF-enriched Li-SEI, ultimately progressing to an anion-dominant r-SEI (LiF and $Li_2S$) with extended cycling, underscoring the dynamic processes shaping SEI formation over time (Figure 2f).

Together, these trends indicate a transition from oxygen-rich interphase components to increasingly dominant anion-derived (LiF and sulfur-containing) species with cycling, linking compositional evolution to interphase restructuring. We note that XPS depth profiling may be affected by preferential sputtering, beam-induced chemical rearrangement, and matrix-dependent sputter rates; therefore, the reported compositions are interpreted as semiquantitative indicators of relative trends rather than absolute stoichiometries.

### 2.3. 3D Li-Metal Plating Drives Nanoscale LiF Domain Segregation

To complement the XPS analyses, we performed nanoscale secondary ion mass spectrometry (NanoSIMS) to map the spatiochemical heterogeneity of various compounds in different SEI types (Figures 3 and S9).[26] Discernible signals of $^7Li^1H^-$ ions were observed on the surfaces of Cu-SEI, Li-SEI-1, and r-SEI-5 samples, which correlated well with the spatial distributions of $^{16}O^-$ and $^{19}F^-$ ions. The presence of LiH, inferred from the low-BE peak at 52.5 eV in the Li 1s spectra (Figure S9), was confirmed by the $^7Li^1H^-$ signal.[22] The $^{16}O^-$ signals primarily originate from $Li_2O$ and LiOH, while the $^{19}F^-$ signals correspond to LiF. Normalized 2D mapping of the $^{19}F^-/^{16}O^-$ ion intensities revealed uniform distributions of both ions across Cu-SEI and r-SEI-5 samples, whereas r-SEI-5 is more F-rich. (Figure 3c and 3i) In contrast, Li-SEI-1 exhibited distinct hotspots, indicating local aggregation of LiF (Figure 3f). This aligns with previous findings from cryogenic electron microscopy (cryo-EM), suggesting that LiF can exist as an indirect SEI phase, not in direct contact with the Li metal.[23] The correlated distributions of $^{16}O^-$ and $^{19}F^-$ ions in other regions of the Li-SEI-1 sample highlight the coexistence of $Li_2O$/LiOH and LiF in the direct monolithic SEI formed from the DME/1 M LiFSI electrolyte.[27] In line with XPS quantification, the similar overall O/F ratios for Li-SEI-1 and r-SEI-5 indicate that the direct passivating SEI on Li metal is enriched in $Li_2O$/LiOH, while the indirect SEI is enriched in LiF.[23] This spatially resolved compositional inhomogeneity in Li-SEI-1 suggests that not all LiF products from $FSI^-$ decomposition are incorporated into the direct passivating SEI.

In contrast, LiF is more uniformly distributed across the entire r-SEI-5 sample. This apparent transition from localized hotspots to a more continuous distribution does not indicate chemical homogenization, but reflects mechanical redistribution of LiF-rich domains during stripping. During intergranular collapse, contraction of lithium drives confinement and coalescence of initially segregated domains.





https://doi.org/10.1021/jacs.6c04430
J. Am. Chem. Soc. 2026, 148, 24084–24095

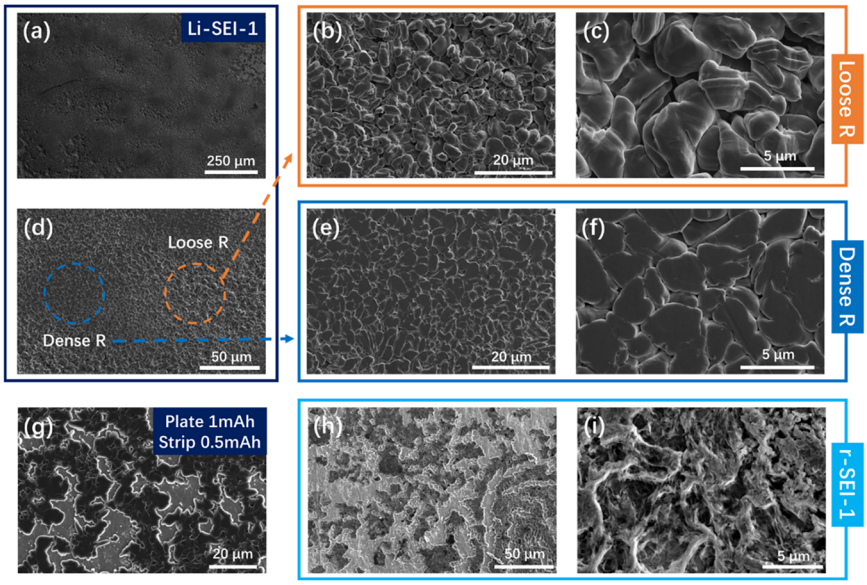


**Figure 4.** SEM comparison of (a–f) Li-SEI-1, (g) Li-SEI-1 after stripping 0.5 mAh of Li, and (h–i) r-SEI-1 samples. Wide-area views of Li-SEI-1 morphology are shown in (a) and (d), with higher-magnification images of loose and dense regions (R) provided in (b, c) and (e, f), respectively. Panels (g–i) illustrate the emergence of the porous residual SEI (r-SEI) following partial or full stripping. All SEM analyses were performed using air-free transfer to avoid atmospheric exposure. The intermediate stripping state (g) highlights the development of intergranular void space, providing evidence for confinement of interphase species during structural evolution.

NanoSIMS provides lateral spatial resolution on the order of ~50–100 nm under the present conditions. The images represent depth-integrated ion intensities accumulated over multiple sputtering cycles, rather than a single well-defined depth slice. All samples were prepared and measured under identical conditions. Pronounced LiF-enriched lateral heterogeneity is observed only for Li-SEI, but not for Cu-SEI or r-SEI, supporting that this feature reflects an intrinsic difference rather than a random local variation. We note that surface topography may influence secondary ion yield and contribute to apparent intensity contrast; however, the LiF-rich domains consistently correlate with compositional trends identified by XPS, supporting their assignment to intrinsic chemical heterogeneity.

Given that LiF hotspots emerge only on Li-SEI formed on three-dimensional Li deposits, these observations indicate that spatially heterogeneous transport environments—arising from intergranular packing and variable electrolyte accessibility—govern the lateral retention of anion-derived species. We further note that NanoSIMS provides lateral (2D) chemical mapping; thus, further spatial interpretation can combine such lateral partitioning with vertical compositional gradients independently inferred from XPS/XAS discussed later. The morphology-linked lateral partitioning observed here may depend on electrolyte chemistry and remains to be explored across systems.

### 2.4. Stripping-Driven Intergranular Collapse Forms a Porous r-SEI Scaffold

To correlate with the above NanoSIMS imaging, we further investigated the morphological evolution of the first-cycle electrodeposited Li metal before and after stripping, using top-view scanning electron microscopy (SEM) images (Figure 4). For Li-SEI-1, low-magnification SEM images (Figure 4a) reveal spatially distributed contrast variations across the surface, with multiple dense and loose regions coexisting, supporting that the observed intergranular structure is representative rather than a localized artifact. Darker regions, with diameters of approximately 50 $\mu$m, exhibit a more compact and dense morphology of Li-metal grains compared to the rest of the sample (Figure 4d–f). Notably, these darker regions are at least 1 order of magnitude larger than the typical pore sizes of the battery separator, thus excluding its influence on the observations.[28] In both the denser and looser regions, the individual Li-metal grains have diameters around 5 $\mu$m (Figure 4c,4f). However, the intergranular distance within the looser region is noticeably larger than in the denser region, where the boundaries of the $Li^0$ grains are closely packed together. The larger intergranular space (IGS) leads to higher electrode porosity and greater infiltration of liquid electrolyte, thereby establishing spatially heterogeneous transport environments across the electrode.[29] These variations in local confinement and electrolyte accessibility provide the physical basis for the preferential retention of less mobile electrolyte-derived species in confined intergranular regions, as reflected in the lateral LiF segregation observed by NanoSIMS.[30]

Moreover, stripping away half of the total Li-metal capacity (0.5 mAh) partially exposes the underlying Cu current collector, while the morphology of the Li grains remains similar to the fully plated state (Figure 4g). Only after the complete stripping of all Li metal in the first cycle does the r-SEI-1, with its distinct morphology, emerge as a microscopically porous and tortuous framework (Figure 4h,i).[7,8] The characteristic length scale of this porous structure appears to be on the order of micrometers and is consistent with intergranular voids between lithium grains, larger than the typical nanometer-scale thickness of compact SEI layers. We note that nanoscale porosity within the SEI cannot be excluded and may coexist with morphology-derived void structures. Importantly, the intermediate-state observations (Figure 4g, ~50% stripping) provide a mechanistic link between spatiochemical segregation during plating and porous r-SEI formation. During partial stripping, the persistence of Li grains alongside the development of intergranular void space suggests


https://doi.org/10.1021/jacs.6c04430
J. Am. Chem. Soc. 2026, 148, 24084–24095

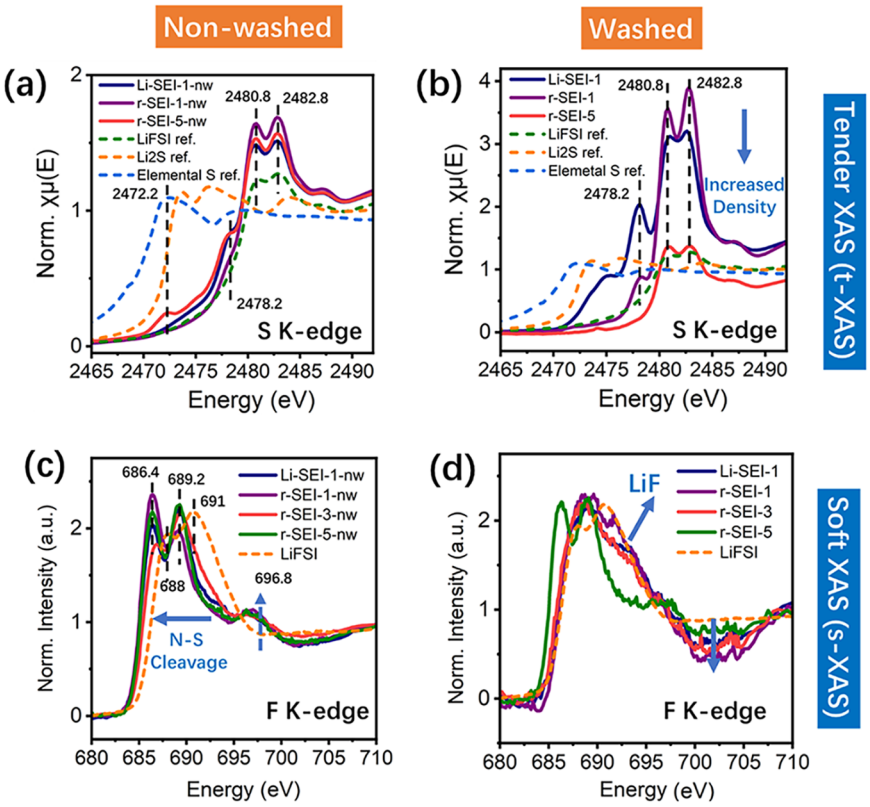


**Figure 5.** (a–d) *Ex situ* X-ray absorption near-edge structure (XANES) spectra comparing (a, b) S K-edge (tender XAS), (c, d) F K-edge (soft XAS) signals for (a, c) nonwashed and (b, d) washed SEI samples.

confinement of these species within contracting intergranular regions. This confinement, coupled with volume contraction, promotes redistribution and consolidation, leading to the porous r-SEI framework observed after complete stripping. Future work combining systematic intermediate-state characterization with correlative chemical mapping would enable fully resolved tracking of domain evolution and distinction between mechanical compaction and chemical precipitation.

We note that this intergranular collapse mechanism primarily describes electrochemically active lithium regions, where stripping-induced volume contraction drives interphase reorganization. In contrast, electronically isolated ("dead") lithium—evidenced by occasional solid particles within the r-SEI framework (Figure S10)—may not undergo contraction and can remain structurally disconnected.

Further Li-metal cycling up to 5 cycles results in a gradual increase in the density of the r-SEI aggregate (Figures S10 and S11), leading to nearly complete coverage of the Cu surface, which correlates with an increase in average CE from <92% to >98%. The emergence of fibrous nanostructures with a diameter of around 100 nm can be attributed to the compact SEI shell that initially passivated the Li filaments. These structures, however, are not observed in the top-view images of Li-SEI-1.[31] The Z-contrast in backscattered (BS-SEM) images of the r-SEI-5 sample further reveals the formation of its interconnected network (Figure S11). Upon the sixth cycle of Li-metal plating, Li-metal grains of similar sizes appear again, despite the accumulation of r-SEI-5 (Figure S12). Notably, the bright spots in the corresponding BS-SEM image indicate the presence of r-SEI within the IGS of different Li-metal grains.

Together, these observations support a morphology-governed mechanism in which three-dimensional lithium growth generates intergranular space (IGS) with heterogeneous confinement, which modulates local transport and species accessibility, ultimately driving the spatially selective retention and lateral segregation of anion-derived interphase products.

### 2.5. Porous r-SEI Retains Electrolyte Beyond Surface-Sensitive Probes

Additionally, we employed synchrotron X-ray absorption spectroscopy (XAS) to investigate the chemical evolution of both Li-SEI and r-SEI during extended cycling (Figure 5). Unlike the surface-sensitive XPS, XAS enables us to analyze chemical changes deeper within the sample.[32−34] Although prolonged XPS sputtering may access deeper regions, it can introduce chemical and structural artifacts;[18] thus, XAS is used as a complementary probe of buried species. We note that XAS measurements focus on representative states and do not include all intermediate samples (e.g., r-SEI-3) due to beamtime constraints. Specifically, tender XAS (t-XAS) in fluorescence yield (FY) mode was used to capture the S K-edge spectra, with a probing depth reaching the micrometer scale. Soft XAS (s-XAS) in total electron yield (TEY) mode was used for both the F and N K-edges, extending the probing depth beyond that of XPS (>5 nm).[35] To examine the impact of LiFSI precipitation on XAS spectra, measurements were conducted on both solvent-washed and nonwashed samples.[18]

For reference, pure LiFSI exhibits two distinctive peaks with a convex shape at 2480.8 and 2482.8 eV (Figure 5a,b). Comparing the XANES spectra of the S K-edge for nonwashed Li-SEI and r-SEI samples reveals prominent LiFSI peaks with comparable intensities, attributed to residual electrolytes on the sample surfaces (Figure 5a). The shoulder peak at 2478.2


https://doi.org/10.1021/jacs.6c04430
J. Am. Chem. Soc. 2026, 148, 24084−24095

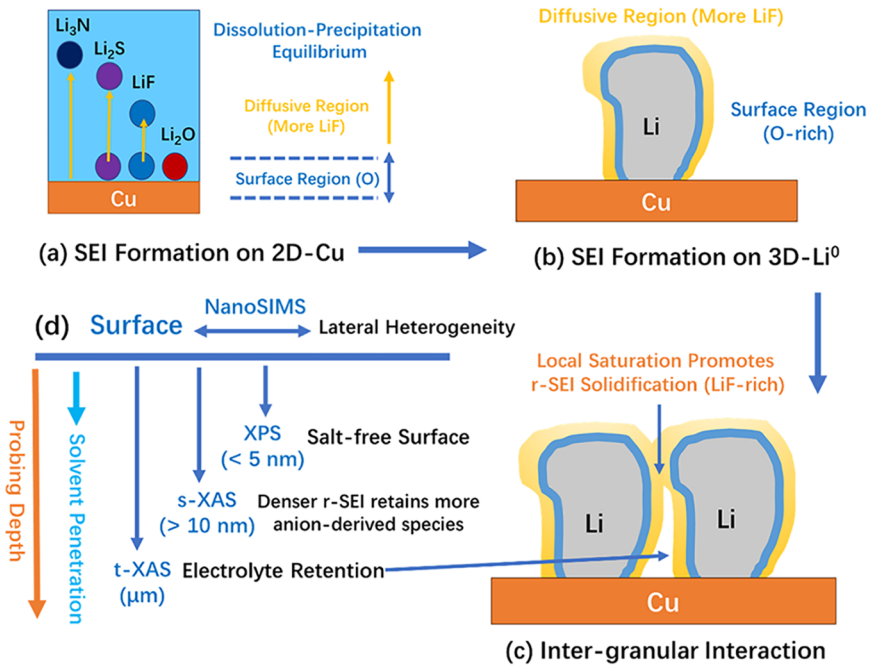


**Figure 6. Spatiochemical evolution of SEI formation from planar Cu to three-dimensional lithium metal.** (a) Bilayer SEI equilibrium model on a two-dimensional (2D) Cu electrode, consisting of a compact, oxygen-rich passivation layer (<10 nm) adjacent to the substrate and an extended diffusive region enriched with soluble or semisoluble anion-derived species, such as LiF, maintained through dissolution−precipitation equilibrium. (b) Upon three-dimensional $Li^0$ nucleation and growth, SEI formation on an individual Li grain becomes laterally heterogeneous, with an oxygen-rich inner layer conformally covering the Li surface and a LiF-rich diffusive outer region extending outward as discrete segregated domains. (c) As multiple $Li^0$ grains grow and approach one another, confinement within the intergranular space (IGS) promotes local saturation and precipitation of electrolyte-derived species, leading to consolidation of a mechanically robust, porous residual SEI (r-SEI) enriched in LiF. (d) Correlative multimodal spectroscopy and imaging (XPS, XAS, and NanoSIMS) links lateral and depth-resolved chemistry by providing complementary information across length scales, showing that solvent washing removes shallow surface salts detectable by XPS, whereas XAS reveals electrolyte-derived species retained deep within the porous interphase, and NanoSIMS captures lateral chemical heterogeneity across the SEI.

eV corresponds to sulfur oxide species ($SO_x$), likely arising from the defluorination of $FSI^-$. Additionally, a significant peak at 2472.2 eV appears specifically for the r-SEI-5-nw sample, indicating the formation of elemental sulfur species ($S_n$) with S−S bonding. Supporting XPS data from an r-SEI-3-nw sample further confirms LiFSI salt accumulation on the surface, with notable S 2p signals also attributable to S−S bond (Figure S13).

After solvent washing, the S K-edge XANES spectra of the SEI samples exhibit significant changes (Figure 5b). Interestingly, the characteristic LiFSI doublet remains detectable across all spectra, despite the absence of LiFSI-related signals at the sample surface in the postwash XPS analysis. The apparently higher normalized intensities of the LiFSI peaks in the r-SEI-1 sample are attributed to enhanced reflection of tender X-rays from the underlying Cu substrate. This effect contrasts with the reduced peak intensities observed in the denser r-SEI-5 sample, where increased material density leads to greater X-ray attenuation. In the washed Li-SEI-1 sample, distinct features associated with $Li_2S$ and $SO_x$ species become more prominent, although their intensities gradually diminish with continued cycling and the evolution toward r-SEI formation.

The F K-edge XANES spectra for pure LiFSI exhibit two distinctive peaks at ∼688 and 691 eV (Figure 5c). In the nonwashed Li-SEI and r-SEI samples, similar double peaks are observed but consistently shift to lower energies, appearing at 686.4 and 689.2 eV, with small shoulder peaks emerging around 696.8 eV. For the N K-edge, pure LiFSI displays a main peak at 403.3 eV and a shoulder at 406.1 eV (Figure S14). By contrast, corresponding peaks in all nonwashed Li-SEI and r-SEI samples shift to higher energies, at 404.4 and 406.9 eV, with new shoulder peaks emerging at the lower energy of 402.8 eV. The opposing shifts observed in the F and N K-edge spectra for FSI-related peaks are attributed to the initial cleavage of N−S bonds in $FSI^-$ anions, leading to the formation of $-SO_2F$ and $-NSO_2F$ fragments. The new low-energy peaks in the N K-edge spectra likely correspond to $Li_3N$ formation, resulting from a second N−S bond cleavage in the $-NSO_2F$ fragment. Based on previous studies, these species ($-SO_2F$, $-NSO_2F$, and $Li_3N$) are considered soluble in liquid electrolytes and are thus less likely to be incorporated directly into the SEI's solid phase.[6]

The washed SEI samples formed during the first three cycles display only broad bands centered around 688.5 eV, attributed to LiF (Figure 5d).[14,36,37] However, after cycling to the fifth cycle, the washed r-SEI-5 sample exhibits nearly identical characteristic peaks at both the F and N K-edges as observed in the nonwashed samples (Figure S15). This indicates that even previously soluble species may integrate into a denser r-SEI matrix, preventing their complete removal through washing.

We note that XAS cannot distinguish between freely confined liquid electrolyte and adsorbed or partially immobilized species, which may include semisoluble decomposition products, precipitated salts in confined regions, or species residing in inaccessible subsurface crevices. Here, "semi-soluble" refers to limited but non-negligible effective mobility of SEI species under electrochemical conditions, rather than




https://doi.org/10.1021/jacs.6c04430
J. Am. Chem. Soc. 2026, 148, 24084−24095

full thermodynamic solubility.[6] Because these features persist after solvent washing yet remain undetectable by surface-sensitive XPS, the observed signals are more generally assigned to retained electrolyte-derived species within the confined porous network of the r-SEI.[35,38,39]

We further note that the washing protocol is intended to remove a substantial fraction of electrolyte-derived species that are accessible to solvent exposure, rather than to preserve the pristine interphase without perturbation. Here, "surface-accessible species" refers to components that can be removed or redistributed under the applied washing conditions. As a result, washed XPS predominantly reflects the composition of species that remain at or near the surface after this treatment, rather than the pristine interphase. In contrast, bulk-sensitive XAS provides complementary information on retained electrolyte-derived species within the interphase. Despite these limitations, the consistent presence of LiFSI-derived features in XAS and their absence in XPS supports the retention of electrolyte-derived species in buried regions.

### 2.6. Spatiochemical Segregation Governs 3D Porous SEI Formation

In our previous work, a planar two-dimensional (2D) Cu electrode was used to establish a bilayer equilibrium model for SEI formation (Figure 6a).[6] In this framework, electrolyte reduction produces SEI components that partition between a thin passivating region (<10 nm) enriched in oxygen-containing inorganic species ($Li_2O$, LiOH) and a more extended diffusive region that contains soluble or semisoluble anion-derived fragments such as $-NSO_2$, $Li_3N$, and $Li_2S$. LiF behaves as a semisoluble component distributed across both regions, reflecting its central yet partially mobile role in interfacial stabilization.

Extending this model to a three-dimensional, dynamically evolving $Li^0$ surface (Figure 6b) reveals a fundamentally different interphase environment. A compact inner SEI still forms directly on $Li^0$, but it is now embedded within a complex outer region shaped by the curvature, roughness, and growth fronts of Li grains. Rather than treating curvature or roughness as independent descriptors, we identify the intergranular space (IGS) formed between adjacent Li grains as the operative structural motif, which governs local confinement, electrolyte accessibility, and transport heterogeneity. Despite these geometric differences, the dominant decomposition pathways remain similar on Cu and $Li^0$, as supported by molecular-dynamics simulations (Figure S16), which show more facile S−F bond cleavage on pristine $Li^0$ relative to a $Li^0$/Cu interface. This promotes LiF formation and yields a stratified SEI with $Li_2O$ concentrated near the substrate and LiF enriched toward the exterior, consistent with our XPS depth profiles.

The critical divergence from the 2D model arises from the fate of anion-derived species in this outer region. On planar Cu, these products remain largely solvated and are removed by washing. On 3D $Li^0$, however, NanoSIMS imaging of Li-SEI-1 reveals pronounced lateral segregation of LiF, forming discrete LiF-rich domains that are spatially decoupled from oxygen-containing phases. This lateral heterogeneity is absent on Cu and represents a fundamentally new behavior of interphase formation unique to three-dimensional lithium metal. The reduced O/F ratio in Li-SEI-1, corroborated by XPS, further reflects preferential LiF accumulation on Li.

This spatial partitioning of compact and diffusive SEI components echoes the inner- and outer-sphere electron-transfer regimes in classical theory.[40] The oxygen-rich interphase adjacent to lithium behaves as a strongly coupled, inner-sphere environment, whereas the more external region—enriched in soluble or semisoluble anion-derived products—acts as a dynamic outer-sphere medium that is continuously reshaped by spatiochemical segregation during three-dimensional lithium growth.

During stripping, consistent with the intermediate-state SEM observations (Figure 4g), contraction of lithium grains mechanically drives the initially segregated anion-derived products into the IGS between neighboring grains (Figure 6c). Progressive confinement reduces the local free volume, which may increase supersaturation and promote redistribution, consolidation, and possible precipitation of semisoluble anion-derived species. This confinement-induced consolidation is consistent with the formation of a continuous, mechanically robust scaffold that persists as the residual SEI (r-SEI). The convergence of O/F ratios between Li-SEI-1 and r-SEI-5 further supports that chemically distinct domains formed during plating are ultimately compacted and integrated into a three-dimensional porous framework. While the present data support structural consolidation during collapse, they do not directly distinguish between mechanical compaction and chemical precipitation pathways.

Morphology corroborates this chemo-mechanical mechanism. SEM shows that initially dense lithium deposits transform into a highly porous, interconnected r-SEI network after complete stripping. These observations suggest that the r-SEI does not originate solely as a surface coating formed at the electrolyte boundary; rather, it develops within the intergranular volume of the lithium matrix and becomes apparent only after removal of the metallic phase. The r-SEI is therefore best understood as an internal scaffold formed at moving grain boundaries during lithium growth and collapse. Future studies under highly kinetic conditions may further clarify the rate dependence of this segregation mechanism.

A key consequence of coupling spatiochemical segregation with intergranular collapse is the emergence of pronounced porosity during cycling. As lithium grains expand laterally from the Cu substrate and then contract during stripping, the segregated, anion-derived inorganic domains entrained within the intergranular space (IGS) consolidate into a robust, porous r-SEI scaffold—consistent with prior reports of cycling-induced interphase densification and restructuring.[21,30,41,42] Depth-resolved spectroscopy highlights the functional impact of this architecture: although XPS confirms effective removal of surface salts after washing, XAS detects electrolyte-derived species retained deep within a confined three-dimensional porous network (Figure 6d).[35] These retained species may contribute to electrolyte decoupling from the bulk reservoir, increased transport tortuosity, and/or impeded subsequent lithium deposition into the IGS, while remaining chemically active toward parasitic pathways such as galvanic corrosion between $Li^0$ and Cu.[43,44] Accordingly, strategies that suppress or delay intergranular collapse, particularly through applied external mechanical pressure as shown in prior studies,[7,30] may improve lithium−metal reversibility and lifetime.

Together, our results show that porous lithium−metal interphases arise from stripping-driven intergranular collapse, while spatiochemical segregation dictates which anion-derived species are concentrated, retained, and solidified within the





https://doi.org/10.1021/jacs.6c04430
J. Am. Chem. Soc. 2026, 148, 24084−24095

collapsing space—a coupled chemo-mechanical mechanism absent on planar Cu and not captured by conventional SEI models. This framework captures the transition from heterogeneous Li-SEI to a more consolidated porous r-SEI that retains electrolyte-derived species. These results suggest that controlling lithium morphology and suppressing intergranular heterogeneity, as well as designing electrolytes and interphases that limit accumulation of partially mobile decomposition products, may represent potential design directions for mitigating pore formation and improving interphase stability. While not directly measured in this study, the proposed interphase structure suggests potential relevance to pressure-dependent lithium−metal performance behavior and transport limitations reported in prior work.[7,30]

## 3. CONCLUSIONS

In summary, our correlative, multilength-scale analysis shows that the lithium−metal SEI evolves through spatiochemical segregation of anion-derived products that is intrinsically coupled to lithium morphology and cycling dynamics, giving rise to porous lithium−metal interphases. Quantitative X-ray photoelectron spectroscopy on rigorously salt-free surfaces resolves distinct compositional trajectories for the Cu-SEI, Li-SEI, and residual SEI (r-SEI) during repeated plating and stripping. Nanoscale secondary ion mass spectrometry reveals that during lithium deposition, $FSI^-$-derived species—dominated by LiF—partition into discrete domains spatially decoupled from oxygen-rich phases at the lithium surface, while synchrotron X-ray absorption spectroscopy detects electrolyte species retained deep within the interphase, consistent with a three-dimensional porous r-SEI. Direct three-dimensional spatial mapping (e.g., tomography) would be required to fully resolve the spatial distribution of these domains.

Collectively, these results support that stripping-induced intergranular contraction creates the porous scaffold, whereas spatiochemical segregation dictates which anion-derived products are concentrated, retained and consolidated within the collapsing intergranular space, thereby governing interphase chemistry, architecture, and transport. This segregation−confinement chemo-mechanical framework clarifies how lithium morphology reshapes interphase evolution and provides design insights that may help mitigate retention of electrolyte-derived species, suppress intergranular porosity, and improve lithium−metal reversibility. More broadly, this morphology−transport coupling provides a practical design lever for regulating interphase stability and long-term performance in lithium−metal batteries. Extending this segregation−confinement mechanism to other electrolyte systems (e.g., fluorinated or high-concentration electrolytes) represents a promising direction for future investigation. More broadly, these findings establish spatiochemical segregation as a governing principle for the chemo-mechanical evolution of dynamically formed electrochemical interphases.

## ■ ASSOCIATED CONTENT

### Supporting Information

The Supporting Information is available free of charge at https://pubs.acs.org/doi/10.1021/jacs.6c04430.

Experimental methods; electrochemical protocols and analysis; XPS sputtering profiles and peak deconvolution (Li 1s, O 1s, C 1s, F 1s, S 2p, N 1s); additional NanoSIMS imaging and analysis; additional SEM characterization; additional XAS measurements and spectra; and AIMD simulation details and results (PDF)

## ■ AUTHOR INFORMATION


### Corresponding Authors

**Yi Cui** − *Department of Materials Science and Engineering and Department of Energy Science and Engineering, Stanford University, Stanford, California 94305, United States; Stanford Institute for Materials and Energy Sciences, SLAC National Accelerator Laboratory, Menlo Park, California 94025, United States;* orcid.org/0000-0002-6103-6352; Email: yicui@stanford.edu

**Zhenan Bao** − *Department of Chemical Engineering, Stanford University, Stanford, California 94305, United States;* orcid.org/0000-0002-0972-1715; Email: zbao@stanford.edu

### Authors

**Weilai Yu** − *Department of Chemical Engineering, Stanford University, Stanford, California 94305, United States; Department of Chemical Engineering and Applied Chemistry, University of Toronto, Toronto, Ontario M5S 3E5, Canada;* orcid.org/0000-0002-9420-0702

**Hao Lyu** − *Department of Chemical Engineering, Stanford University, Stanford, California 94305, United States;* orcid.org/0000-0001-7393-2456

**Donglin Li** − *Department of Materials Science and Engineering, Stanford University, Stanford, California 94305, United States*

**Kuan-Yu Lin** − *Department of Chemical Engineering, Stanford University, Stanford, California 94305, United States*

**Jacob Florian** − *Department of Chemical Engineering, Stanford University, Stanford, California 94305, United States;* orcid.org/0000-0003-1895-8463

**Yukio Cho** − *Department of Chemical Engineering, Stanford University, Stanford, California 94305, United States; SLAC-Stanford Battery Center, SLAC National Accelerator Laboratory, Menlo Park, California 94025, United States;* orcid.org/0000-0003-0919-692X

**Xin Xu** − *Department of Materials Science and Engineering, Stanford University, Stanford, California 94305, United States; The Polytechnic School, Arizona State University, Mesa, Arizona 85212, United States*

**Yuelang Chen** − *Department of Chemical Engineering, Stanford University, Stanford, California 94305, United States; Department of Chemistry, Stanford University, Stanford, California 94305, United States;* orcid.org/0000-0002-5249-0596

**Hongchang Hao** − *Department of Materials Science and Engineering, Stanford University, Stanford, California 94305, United States; SLAC-Stanford Battery Center, SLAC National Accelerator Laboratory, Menlo Park, California 94025, United States*

**Chengyi Xu** − *Department of Chemical Engineering, Stanford University, Stanford, California 94305, United States*

**Dennis Nordlund** − *Stanford Synchrotron Radiation Lightsource, SLAC National Accelerator Laboratory, Menlo Park, California 94025, United States*

**Jagjit Nanda** − *Department of Materials Science and Engineering, Stanford University, Stanford, California 94305,*

*United States; SLAC-Stanford Battery Center, SLAC National Accelerator Laboratory, Menlo Park, California 94025, United States;* orcid.org/0000-0002-6875-0057

**Jian Qin** − *Department of Chemical Engineering, Stanford University, Stanford, California 94305, United States;* orcid.org/0000-0001-6271-068X

Complete contact information is available at: https://pubs.acs.org/10.1021/jacs.6c04430

## Notes

The authors declare no competing financial interest.

## ■ ACKNOWLEDGMENTS

This work was supported by the U.S. Department of Energy, Office of Energy Efficiency and Renewable Energy, Vehicle Technologies Office, through the Battery Materials Research Program and the Battery500 Consortium. A portion of this research was carried out at the Stanford Nano Shared Facilities, supported by the National Science Foundation under Award No. ECCS-2026822. We thank Erik Nelson for his assistance at Beamline 4-3 of the Stanford Synchrotron Radiation Lightsource (SSRL). Use of SSRL at SLAC National Accelerator Laboratory is supported by the U.S. Department of Energy, Office of Science, Office of Basic Energy Sciences, under Contract No. DE-AC02-76SF00515.

## ■ REFERENCES

(1) Liu, J.; Bao, Z.; Cui, Y.; Dufek, E. J.; Goodenough, J. B.; Khalifah, P.; Li, Q.; Liaw, B. Y.; Liu, P.; Manthiram, A.; Meng, Y. S.; Subramanian, V. R.; Toney, M. F.; Viswanathan, V. V.; Whittingham, M. S.; Xiao, J.; Xu, W.; Yang, J.; Yang, X.-Q.; Zhang, J.-G. Pathways for Practical High-Energy Long-Cycling Lithium Metal Batteries. *Nat. Energy* **2019**, *4* (3), 180−186.

(2) Zhang, J.-G. Anode-Less. *Nat. Energy* **2019**, *4* (8), 637−638.

(3) Lin, D.; Liu, Y.; Cui, Y. Reviving the Lithium Metal Anode for High-Energy Batteries. *Nat. Nanotechnol.* **2017**, *12* (3), 194−206.

(4) Xu, K. Interfaces and Interphases in Batteries. *J. Power Sources* **2023**, *559*, No. 232652.

(5) Xu, K. *Electrolytes, Interfaces and Interphases: Fundamentals and Applications in Batteries*; Royal Society of Chemistry: London, 2023.

(6) Yu, W.; Lin, K.-Y.; Boyle, D. T.; Tang, M. T.; Cui, Y.; Chen, Y.; Yu, Z.; Xu, R.; Lin, Y.; Feng, G.; Huang, Z.; Michalek, L.; Li, W.; Harris, S. J.; Jiang, J.-C.; Abild-Pedersen, F.; Qin, J.; Cui, Y.; Bao, Z. Electrochemical Formation of Bis(Fluorosulfonyl)Imide-Derived Solid-Electrolyte Interphase at Li-Metal Potential. *Nat. Chem.* **2025**, *17* (2), 246−255.

(7) Wang, H.; Huang, W.; Yu, Z.; Huang, W.; Xu, R.; Zhang, Z.; Bao, Z.; Cui, Y. Efficient Lithium Metal Cycling over a Wide Range of Pressures from an Anion-Derived Solid-Electrolyte Interphase Framework. *ACS Energy Lett.* **2021**, *6* (2), 816−825.

(8) Chen, Y.; Yu, Z.; Gong, H.; Zhang, W.; Rudnicki, P. E.; Huang, Z.; Yu, W.; Kim, S. C.; Boyle, D. T.; Sayavong, P.; Celik, H.; Xu, R.; Lin, Y.; Wang, S.; Qin, J.; Cui, Y.; Bao, Z. Failure Process During Fast Charging of Lithium Metal Batteries with Weakly Solvating Fluoroether Electrolytes. *J. Phys. Chem. C* **2024**, *128* (28), 11487−11497.

(9) Tan, S.; Kim, J.-M.; Corrao, A.; Ghose, S.; Zhong, H.; Rui, N.; Wang, X.; Senanayake, S.; Polzin, B. J.; Khalifah, P.; Xiao, J.; Liu, J.; Xu, K.; Yang, X.-Q.; Cao, X.; Hu, E. Unravelling the Convoluted and Dynamic Interphasial Mechanisms on Li Metal Anodes. *Nat. Nanotechnol.* **2023**, *18* (3), 243−249.

(10) Hobold, G. M.; Wang, C.; Steinberg, K.; Li, Y.; Gallant, B. M. High Lithium Oxide Prevalence in the Lithium Solid−Electrolyte Interphase for High Coulombic Efficiency. *Nat. Energy* **2024**, *9* (5), 580−591.

(11) Wang, H.; Yu, Z.; Kong, X.; Kim, S. C.; Boyle, D. T.; Qin, J.; Bao, Z.; Cui, Y. Liquid Electrolyte: The Nexus of Practical Lithium Metal Batteries. *Joule* **2022**, *6* (3), 588−616.

(12) Yu, Z.; Wang, H.; Kong, X.; Huang, W.; Tsao, Y.; Mackanic, D. G.; Wang, K.; Wang, X.; Huang, W.; Choudhury, S.; Zheng, Y.; Amanchukwu, C. V.; Hung, S. T.; Ma, Y.; Lomeli, E. G.; Qin, J.; Cui, Y.; Bao, Z. Molecular Design for Electrolyte Solvents Enabling Energy-Dense and Long-Cycling Lithium Metal Batteries. *Nat. Energy* **2020**, *5* (7), 526−533.

(13) Yu, Z.; Rudnicki, P. E.; Zhang, Z.; Huang, Z.; Celik, H.; Oyakhire, S. T.; Chen, Y.; Kong, X.; Kim, S. C.; Xiao, X.; Wang, H.; Zheng, Y.; Kamat, G. A.; Kim, M. S.; Bent, S. F.; Qin, J.; Cui, Y.; Bao, Z. Rational Solvent Molecule Tuning for High-Performance Lithium Metal Battery Electrolytes. *Nat. Energy* **2022**, *7* (1), 94−106.

(14) Tan, S.; Kuai, D.; Yu, Z.; Perez-Beltran, S.; Rahman, M. M.; Xia, K.; Wang, N.; Chen, Y.; Yang, X.-Q.; Xiao, J.; Liu, J.; Cui, Y.; Bao, Z.; Balbuena, P. B.; Hu, E. Evolution and Interplay of Lithium Metal Interphase Components Revealed by Experimental and Theoretical Studies. *J. Am. Chem. Soc.* **2024**, *146* (17), 11711−11718.

(15) Zachman, M. J.; Tu, Z.; Choudhury, S.; Archer, L. A.; Kourkoutis, L. F. Cryo-STEM Mapping of Solid−Liquid Interfaces and Dendrites in Lithium-Metal Batteries. *Nature* **2018**, *560* (7718), 345−349.

(16) Zhang, Z.; Li, Y.; Xu, R.; Zhou, W.; Li, Y.; Oyakhire, S. T.; Wu, Y.; Xu, J.; Wang, H.; Yu, Z.; Boyle, D. T.; Huang, W.; Ye, Y.; Chen, H.; Wan, J.; Bao, Z.; Chiu, W.; Cui, Y. Capturing the Swelling of Solid-Electrolyte Interphase in Lithium Metal Batteries. *Science* **2022**, *375* (6576), 66−70.

(17) Menkin, S.; O'Keefe, C. A.; Gunnarsdóttir, A. B.; Dey, S.; Pesci, F. M.; Shen, Z.; Aguadero, A.; Grey, C. P. Toward an Understanding of SEI Formation and Lithium Plating on Copper in Anode-Free Batteries. *J. Phys. Chem. C* **2021**, *125* (30), 16719−16732.

(18) Yu, W.; Yu, Z.; Cui, Y.; Bao, Z. Degradation and Speciation of Li Salts during XPS Analysis for Battery Research. *ACS Energy Lett.* **2022**, *7*, 3270−3275.

(19) Shterenberg, I.; Salama, M.; Gofer, Y.; Aurbach, D. X-Ray Photodecomposition of Bis(Trifluoromethanesulfonyl)Imide, Bis-(Fluorosulfonyl)Imide, and Hexafluorophosphate. *J. Phys. Chem. C* **2017**, *121* (7), 3744−3751.

(20) Wood, K. N.; Teeter, G. XPS on Li-Battery-Related Compounds: Analysis of Inorganic SEI Phases and a Methodology for Charge Correction. *ACS Appl. Energy Mater.* **2018**, *1* (9), 4493−4504.

(21) Fang, C.; Li, J.; Zhang, M.; Zhang, Y.; Yang, F.; Lee, J. Z.; Lee, M.-H.; Alvarado, J.; Schroeder, M. A.; Yang, Y.; Lu, B.; Williams, N.; Ceja, M.; Yang, L.; Cai, M.; Gu, J.; Xu, K.; Wang, X.; Meng, Y. S. Quantifying Inactive Lithium in Lithium Metal Batteries. *Nature* **2019**, *572* (7770), 511−515.

(22) Shadike, Z.; Lee, H.; Borodin, O.; Cao, X.; Fan, X.; Wang, X.; Lin, R.; Bak, S.-M.; Ghose, S.; Xu, K.; Wang, C.; Liu, J.; Xiao, J.; Yang, X.-Q.; Hu, E. Identification of LiH and Nanocrystalline LiF in the Solid−Electrolyte Interphase of Lithium Metal Anodes. *Nat. Nanotechnol.* **2021**, *16* (5), 549−554.

(23) Huang, W.; Wang, H.; Boyle, D. T.; Li, Y.; Cui, Y. Resolving Nanoscopic and Mesoscopic Heterogeneity of Fluorinated Species in Battery Solid-Electrolyte Interphases by Cryogenic Electron Microscopy. *ACS Energy Lett.* **2020**, *5* (4), 1128−1135.

(24) Heiskanen, S. K.; Kim, J.; Lucht, B. L. Generation and Evolution of the Solid Electrolyte Interphase of Lithium-Ion Batteries. *Joule* **2019**, *3* (10), 2322−2333.

(25) Oyakhire, S. T.; Gong, H.; Cui, Y.; Bao, Z.; Bent, S. F. An X-Ray Photoelectron Spectroscopy Primer for Solid Electrolyte Interphase Characterization in Lithium Metal Anodes. *ACS Energy Lett.* **2022**, *7* (8), 2540−2546.

(26) Li, K.; Liu, J.; Grovenor, C. R. M.; Moore, K. L. NanoSIMS Imaging and Analysis in Materials Science. *Annu. Rev. Anal. Chem.* **2020**, *13* (1), 273−292.

(27) Cao, X.; Ren, X.; Zou, L.; Engelhard, M. H.; Huang, W.; Wang, H.; Matthews, B. E.; Lee, H.; Niu, C.; Arey, B. W.; Cui, Y.; Wang, C.;

Xiao, J.; Liu, J.; Xu, W.; Zhang, J.-G. Monolithic Solid−Electrolyte Interphases Formed in Fluorinated Orthoformate-Based Electrolytes Minimize Li Depletion and Pulverization. *Nat. Energy* **2019**, *4* (9), 796−805.
(28) Mun, S. C.; Won, J. H. Manufacturing Processes of Microporous Polyolefin Separators for Lithium-Ion Batteries and Correlations between Mechanical and Physical Properties. *Crystals* **2021**, *11* (9), No. 1013.
(29) Lu, B.; Li, W.; Cheng, D.; Bhamwala, B.; Ceja, M.; Bao, W.; Fang, C.; Meng, Y. S. Suppressing Chemical Corrosions of Lithium Metal Anodes. *Adv. Energy Mater.* **2022**, *12* (48), No. 2202012.
(30) Fang, C.; Lu, B.; Pawar, G.; Zhang, M.; Cheng, D.; Chen, S.; Ceja, M.; Doux, J.-M.; Musrock, H.; Cai, M.; Liaw, B.; Meng, Y. S. Pressure-Tailored Lithium Deposition and Dissolution in Lithium Metal Batteries. *Nat. Energy* **2021**, *6* (10), 987−994.
(31) Li, Y.; Huang, W.; Li, Y.; Pei, A.; Boyle, D. T.; Cui, Y. Correlating Structure and Function of Battery Interphases at Atomic Resolution Using Cryoelectron Microscopy. *Joule* **2018**, *2* (10), 2167−2177.
(32) Lin, F.; Nordlund, D.; Markus, I. M.; Weng, T.-C.; Xin, H. L.; Doeff, M. M. Profiling the Nanoscale Gradient in Stoichiometric Layered Cathode Particles for Lithium-Ion Batteries. *Energy Environ. Sci.* **2014**, *7* (9), 3077−3085.
(33) Gao, X.; Zheng, X.; Tsao, Y.; Zhang, P.; Xiao, X.; Ye, Y.; Li, J.; Yang, Y.; Xu, R.; Bao, Z.; Cui, Y. All-Solid-State Lithium−Sulfur Batteries Enhanced by Redox Mediators. *J. Am. Chem. Soc.* **2021**, *143* (43), 18188−18195.
(34) Mu, L.; Feng, X.; Kou, R.; Zhang, Y.; Guo, H.; Tian, C.; Sun, C.; Du, X.; Nordlund, D.; Xin, H. L.; Lin, F. Deciphering the Cathode−Electrolyte Interfacial Chemistry in Sodium Layered Cathode Materials. *Adv. Energy Mater.* **2018**, *8* (34), No. 1801975.
(35) Ketenoglu, D. A General Overview and Comparative Interpretation on Element-Specific X-Ray Spectroscopy Techniques: XPS, XAS, and XRS. *X-Ray Spectrometry* **2022**, *51* (5−6), 422−443.
(36) Shadike, Z.; Tan, S.; Lin, R.; Cao, X.; Hu, E.; Yang, X.-Q. Engineering and Characterization of Interphases for Lithium Metal Anodes. *Chem. Sci.* **2022**, *13* (6), 1547−1568.
(37) Balasubramanian, M.; Lee, H. S.; Sun, X.; Yang, X. Q.; Moodenbaugh, A. R.; McBreen, J.; Fischer, D. A.; Fu, Z. Formation of SEI on Cycled Lithium-Ion Battery Cathodes: Soft X-Ray Absorption Study. *Electrochem. Solid-State Lett.* **2002**, *5* (1), A22−A25.
(38) Tanuma, S.; Powell, C. J.; Penn, D. R. Calculation of Electron Inelastic Mean Free Paths (IMFPs) VII. Reliability of the TPP-2M IMFP Predictive Equation. *Surf. Interface Anal.* **2003**, *35* (3), 268−275.
(39) Tanuma, S.; Powell, C. J.; Penn, D. R. Calculations of Electron Inelastic Mean Free Paths for 31 Materials. *Surf. Interface Anal.* **1988**, *11* (11), 577−589.
(40) Marcus, R. A. Electron Transfer Reactions in Chemistry: Theory and Experiment (Nobel Lecture). *Angew. Chem., Int. Ed.* **1993**, *32* (8), 1111−1121.
(41) Wang, X.; Pawar, G.; Li, Y.; Ren, X.; Zhang, M.; Lu, B.; Banerjee, A.; Liu, P.; Dufek, E. J.; Zhang, J.-G.; Xiao, J.; Liu, J.; Meng, Y. S.; Liaw, B. Glassy Li Metal Anode for High-Performance Rechargeable Li Batteries. *Nat. Mater.* **2020**, *19* (12), 1339−1345.
(42) Zhao, Q.; Deng, Y.; Utomo, N. W.; Zheng, J.; Biswal, P.; Yin, J.; Archer, L. A. On the Crystallography and Reversibility of Lithium Electrodeposits at Ultrahigh Capacity. *Nat. Commun.* **2021**, *12* (1), No. 6034.
(43) Lin, D.; Liu, Y.; Li, Y.; Li, Y.; Pei, A.; Xie, J.; Huang, W.; Cui, Y. Fast Galvanic Lithium Corrosion Involving a Kirkendall-Type Mechanism. *Nat. Chem.* **2019**, *11* (4), 382−389.
(44) Boyle, D. T.; Huang, W.; Wang, H.; Li, Y.; Chen, H.; Yu, Z.; Zhang, W.; Bao, Z.; Cui, Y. Corrosion of Lithium Metal Anodes during Calendar Ageing and Its Microscopic Origins. *Nat. Energy* **2021**, *6* (5), 487−494.





https://doi.org/10.1021/jacs.6c04430
J. Am. Chem. Soc. 2026, 148, 24084−24095